energies

MDPI

Article

Effect of the Density Ratio on Emulsions and Their Segregation: A Direct Numerical Simulation Study

Oscar Krzeczek, Theresa Trummler †, Elias Trautner and Markus Klein *

Institute of Applied Mathematics and Scientific Computing, University of the Bundeswehr Munich, Werner-Heisenberg-Weg 39, 85577 Neubiberg, Germany

* Correspondence: markus.klein@unibw.de

† Current address: MTU Aero Engines AG, Dachauer Str. 665, 80995 Munich, Germany.

Abstract: Using direct numerical simulation (DNS) in combination with the volume of fluid method (VoF), we investigate the influence of the density ratio between the carrier and dispersed phase on emulsions, where the baseline simulation approximately corresponds to the ratio of water-in-gasoline emulsions. For this purpose, homogeneous isotropic turbulence (HIT) is generated using a linear forcing method, enhanced by a proportional–integral–derivative (PID) controller, ensuring a constant turbulent kinetic energy (TKE) for two-phase flows, where the TKE balance equation contains an additional term due to surface tension. Then, the forcing is stopped, and gravitational acceleration is activated. The proposed computational setup represents a unique and well-controlled configuration to study emulsification and segregation. We consider four different density ratios, which are applied in industrial processes, to investigate the influence of the density ratio on the statistically steady state of the emulsions, and their segregation under decaying turbulence and constant gravitational acceleration. At the statistically steady state, we hold the turbulence constant and study the effects of the density ratio ρ_d/ρ_c, on the interface area, the Sauter mean diameter (SMD), and the statistical droplet size distribution. We find that all are affected by the density ratio, and we observe a relation between the SMD and ρ_d/ρ_c. Furthermore, we assume a dependence of the critical Weber number on the density ratio. In the second part of our work, we study the segregation process. To this end, we consider the change in the center of mass of the disperse phase and the energy release, to analyze the dependence of segregation on the density difference $\Delta\rho/\rho_d$. We show that segregation scales with the density difference and the droplet size, and a segregation time scale has been suggested that collapses the height of the center of mass for different density ratios.

Keywords: direct numerical simulations; emulsions; segregation; density effect; computational fluid dynamics

Citation: Krzeczek, O.; Trummler, T.; Trautner, E.; Klein, M. Effect of the Density Ratio on Emulsions and Their Segregation: A Direct Numerical Simulation Study. *Energies* **2023**, *16*, 3160. https://doi.org/10.3390/en16073160

Academic Editor: Dmitry Eskin

Received: 26 February 2023
Revised: 19 March 2023
Accepted: 29 March 2023
Published: 31 March 2023

1. Introduction

Emulsions are suspensions of non-miscible liquids (e.g., water in gasoline) and play an essential role in various industrial applications, e.g., pharmaceuticals [1], food processing [2], and oil production [3–5]. Of particular interest, is the use of water-in-gasoline emulsions in gasoline-water direct injection (GWDI), which is considered a key technology for the future of the automobile industry, to reduce emissions and thus to counteract the climate crisis. Experimental work [6] demonstrated that GWDI could save up to 12% in fuel, while reducing CO_2 emissions.

Numerical methods can be used to gain knowledge for different applications, which can then be used in industrial processes. Therefore, studying turbulent emulsions in a steady state and their segregation under the influence of gravity, is essential. Furthermore, it is necessary to identify correlations and verify the validity of existing scaling laws. Important for turbulent emulsions, is the distribution of droplet sizes around the Hinze scale, according to the research results of Deane and Stokes [7]. They investigated the

bubble formation mechanisms in breaking waves, as well as the correlation of bubble sizes and energy dissipation proposed by Garret et al. [8]. However, the scaling laws of droplet distribution are not yet fully understood and require further discussion [9,10].

Research activities in recent years reflect the importance of emulsions. Pacek et al. [11] and Kraume et al. [12], used turbulent emulsions in a stirred vessel to study the relations between SMD and volume fraction. Keogl et al. [13], studied the properties of the disperse phase in water-in-ethanol emulsions, using laser-induced fluorescence. The focus of most of the studies has been on the evaluation of the statistical distribution of droplet sizes. The segregation process of emulsions under gravity has also been studied experimentally. The focus here has been on investigating gravity settler models for water separation in oil production. For example, the models deliver correlations for the temporal evolution of zone heights, and were listed by Frising et al. [14]. Because of the complexity of these experiments, and the challenging modeling, numerical studies of the segregation process are an optimal complement. Trummler et al. [15] investigated the segregation process of oil-in-water emulsions, by varying the surface tension and the gravitational acceleration using DNS. They proposed a dimensionless segregation number, that characterizes the relationship between the release of potential energy and the release of surface energy. Moreover, they have also defined a characteristic time scale for segregation and conjectured that the average rising velocity of the lighter phase, scales with the dimensionless density difference $\Delta\rho/\rho_d$, and depends on the droplet size.

There is a large number of numerical studies on turbulent emulsions. Using DNS, Perlekar et al. [16] studied the droplet size distribution in homogeneous isotropic turbulence, with a pseudopotential Lattice–Boltzmann method. They report that probability density functions of droplet radii follow a log-normal distribution, and that the Hinze criterion is well-satisfied at a small volume fraction, while a departure is observed at higher volume fractions. Mukherjee et al. [17] used an improved pseudopotential Lattice–Boltzmann method for the analysis. A generalization of the Hinze scale is proposed, based on the Weber number spectrum, which applies also to dense suspensions. In addition, they report that the flow topology of emulsions is different to single phase turbulence. Dodd and Ferrante [18] showed the relationship between turbulent kinetic energy evolution and droplet deformation, breakup, and coalescence processes in decaying isotropic turbulence, for a range of different Weber numbers and density and viscosity ratios. Crealesi-Esposito et al. [10] and Begemann et al. [9] studied emulsions using the VoF method, which is also applied in this work. Crealesi-Esposito et al. [10] varied the volume fractions, viscosity ratio, and surface tension. Their work shows that energy is transported consistently from large to small scales by the interface without an inverse cascade, and that the total surface is found to be directly proportional to the amount of energy transported. Begemann et al. [9] studied emulsions at different turbulent kinetic energies and surface tensions. Additionally, they demonstrated the applicability of Lundgren forcing [19], with a modification suggested by Carrol and Blanquart [20], and an additional PID controller, also used in this work.

Since many recent numerical studies on turbulent emulsions assume identical densities [10,16,17,21] of the dispersed and carrier phases, the influence of the density ratio has to be investigated in more detail. Moreover, numerical studies on emulsions in the literature focus on the droplet size distribution or the characterization of the steady state [10,16–18,21,22], but typically not on segregation. In summary, we are not aware of any numerical analyses of different density ratios in the segregation process, and numerical studies are the ideal tool for varying a single parameter while keeping all the others unchanged. The present work addresses this gap in the existing literature.

In this respect, the main objectives of the present work are: (i) to analyze the effect of the density ratio on the droplet sizes and their statistical distribution in the statistically steady state, (ii) to consider the effects of density ratio on the segregation process, due to the change in the center of mass of the disperse phase and the release of energy, (iii) to review the time scale proposed by Trummler et al. [15] for the segregation process.

This work is structured as follows. In Section 2, we explain the governing equations and the flow solver, which we use for numerical analysis. In Section 3, we describe the configurations considered in the statistically steady state and during segregation. Moreover, the droplet detection algorithm is explained. The simulation procedure and the forcing method used are also described in detail. Next, we discuss in Section 4 the effect of the density ratio on the emulsions in HIT. In Section 5, we analyze the different cases under decaying turbulence. Finally, we summarize the results in Section 6 and draw conclusions.

2. Governing Equations and Flow Solver

The simulations are conducted using the open-source code PARIS (parallel, robust, interface simulator) [23]. The flow solver uses the one-fluid formulation [24] of the incompressible Navier–Stokes equations. The continuity and momentum equations can be written as

$$\frac{\partial u_i}{\partial x_i} = 0\,, \tag{1}$$

$$\rho\left(\frac{\partial u_i}{\partial t} + \frac{\partial u_i u_j}{\partial x_j}\right) = -\frac{\partial p}{\partial x_i} + \frac{\partial}{\partial x_j}\left[\mu\left(\frac{\partial u_i}{\partial x_j} + \frac{\partial u_j}{\partial x_i}\right)\right] + \sigma n_i \kappa \delta_s + \rho g_i \tag{2}$$

with the dynamic viscosity μ, the pressure p, the density ρ, the ith velocity component u_i, and the gravitational acceleration g_i. The density and viscosity values are linearly interpolated in each cell, using the local volume fraction α of the dispersed phase, which is identified with the geometrical VoF method [25]

$$\rho = \alpha\rho_d + (1-\alpha)\rho_c, \quad \mu = \alpha\mu_d + (1-\alpha)\mu_c. \tag{3}$$

The indices c and d denote the dispersed and carrier phases, respectively. According to the continuous surface force (CSF) approach [26], the surface tension force is determined from the surface tension coefficient σ, the interface normal $n_i = \frac{\partial \alpha}{\partial x_i}/|\nabla\alpha|$, the interface indicator function $\delta_S = |\nabla\alpha|$, and the interface curvature $\kappa = \frac{\partial n_i}{\partial x_i}$. A state-of-the-art height function approach [27] is used for this calculation. Details of its implementation in PARIS can be found in Aniszewski et al. [23]. The advection of the VoF marker function is performed using a geometric interface reconstruction algorithm, which solves the equation

$$\frac{\partial \alpha}{\partial t} + u_i \frac{\partial \alpha}{\partial x_i} = 0, \quad \alpha = \begin{cases} 1, & \text{if } \boldsymbol{x} \text{ is in dispersed phase.} \\ 0, & \text{if } \boldsymbol{x} \text{ is in carrier phase.} \end{cases} \tag{4}$$

The projection method is used to determine the solution of the Poisson equation for pressure, using a red–black Gauss–Seidel method with over-relaxation (SOR). The temporal derivatives are solved using a second-order predictor–corrector method. A cubic equidistant grid is used for spatial discretization. The convective term of the momentum equation (see Equation (2)) is solved with a third-order QUICK (quadratic upstream interpolation for convective kinematics) [28] scheme. The viscous term is solved with a second-order central difference scheme.

The above mathematical model has been established during the last decade and has been applied to a large number of two-phase flow problems in the literature [29–35]. In addition, the recent paper by the code developers [23], includes a wide variety of well-known test cases such as Poiseuille flow, capillary waves, oscillating droplets and bubbles, and a falling raindrop.

3. Numerical Setup

3.1. Considered Configurations

In our study, we investigate the influence of different density ratios, ρ_d/ρ_c and $\Delta\rho/\rho_d$, on the statistically steady state of emulsions and their segregation under gravity. An essential value for characterizing emulsions is the Hinze scale d_H [36]. The Hinze scale is

defined as the maximum stable diameter of emulsions in HIT, and can be written as follows

$$d_H = \left(\frac{We_{d,crit}}{2}\right)^{3/5} \left(\frac{\rho_c}{\sigma}\right)^{-3/5} \epsilon^{-2/5}. \quad (5)$$

Hence, d_H depends on the dissipation rate ϵ, the density of the carrier phase ρ_c, and the critical Weber number $We_{d,crit}$, which is assumed to be 1.17, following Hinze [36]. This value has been confirmed in numerical work [16] and experimental studies [37].

To characterize the droplet size distribution of the disperse phase, we consider the SMD:

$$d_{32} = \frac{6V_d}{A}, \quad (6)$$

where A is the interface area and V_d is the volume of the disperse phase. This diameter represents a characteristic value of the droplet size distribution and is used to describe dispersions (see [11,12]). Dispersions are generally heterogeneous mixtures and, in contrast to emulsions, not limited to liquid–liquid phases.

Our PID-enhanced forcing method [9] ensures a constant turbulent kinetic energy k for two-phase flows (where the TKE balance equation contains an additional term due to surface tension), which, assuming isotropic turbulence, can be written as $k = \frac{3}{2}u'^2$, where u' is the velocity fluctuation. Furthermore, following Rosales and Meneveau [38], the integral length scale is $L_t = 0.2L$, where L is the domain size. The dissipation rate ϵ, results from the relation $L_t = (u'^2)^{\frac{3}{2}}/\epsilon$. The eddy turn-over time $\tau = k/\epsilon$, for the statistically steady state, is obtained from these relationships. To characterize the turbulent emulsions, we use dimensionless numbers: the Weber number, with the integral length scale $We_l = \rho_c(u')^2 L_t/\sigma$, the turbulent Reynolds number $Re_l = u' L_t/\nu$, and the Taylor Reynolds number $Re_\lambda = u'\lambda/\nu$, with the Taylor microscale $\lambda = \sqrt{15\nu/\epsilon}u'$.

The volume fraction $\Phi = 0.125$, is constant in this study. The domain size L equals 2π, corresponding to a total domain volume of $V = (2\pi)^3$. We use periodic boundary conditions in each direction.

A completely segregated state is assumed as a reference for the interface area, $A_\infty = L^2 = (2\pi)^2$. The resolution of the grid was determined according to the criterion $K_{max}\eta \geq 1.5$ [39]. Here, K_{max} is the maximum wavenumber and is calculated from the number of cells in one direction N and the domain size, via $K_{max} = N\pi/L$. η denotes the Kolmogorov microscale and is defined as $\eta = \left(\nu^3/\epsilon\right)^{1/4}$. $N = 512$ was chosen for all simulations performed in this study, to meet the resolution criterion. The total number of cells is $\approx 1.34 \times 10^8$. We set the TKE at $k = 0.5\,\mathrm{m}^2/\mathrm{s}^2$. This leads to $\epsilon = 0.153\,\mathrm{m}^2/\mathrm{s}^3$ and $\tau = 3.2648\,\mathrm{s}$. An identical surface tension coefficient $\sigma = 0.006\,\mathrm{N/m}$, is assumed for all cases. The ratio of the two kinematic viscosities is $\nu_d/\nu_c = 1$, since $\nu_d = \nu_c = 0.001\,\mathrm{m}^2/\mathrm{s}$. The Hinze scale (Equation (5)) $d_H = 0.071\,\mathrm{m}$, is constant during the forcing phase. Table 1 lists the parameters which remain unchanged in all configurations.

Table 1. Constant parameters for all configurations.

Φ -	ρ_c kg/m^3	τ s	σ N/m	ν_c/ν_d -	k m^2/s^2	ϵ m^2/s^3	Re_λ -	Re_l -	We_l -	L m	N -	d_H m
1/8	1	3.27	0.006	1	0.5	0.153	104	726	70	2π	512	0.071

The density of the carrier phase is $\rho_c = 1\,\mathrm{kg/m}^3$ in all configurations. We define the density ratio $\rho_d/\rho_c = 1.\overline{3}$ as a reference case (*Refcase*), since it approximately corresponds to the ratio of water-in-gasoline emulsions [40]. This value was increased and decreased by a factor of 1.2 for comparison, resulting in the density ratios $1.\overline{1}$ and 1.6.

Furthermore, these cases are compared with the density ratio from the work of Begemann et al. [9], with $\rho_d/\rho_c = 0.9$, where the disperse phase is lighter than the carrier phase. Note that, for the segregation process, the ratio $\Delta\rho/\rho_d$ is the relevant factor, with $\Delta\rho = \rho_d - \rho_c$.

Table 2 gives an overview of the simulations performed with the different physical parameters, and contains examples of practical applications of the studied density ratios.

Table 2. Considered cases.

Case	ρ_d/ρ_c -	$\Delta\rho/\rho_d$ -	$\Delta\rho$ kg/m^3	Example
Refcase	$1.\overline{3}$	$1/4 = 0.25$	$0.\overline{3}$	water-in-gasoline
Reverse-Low Ratio	0.9	$-1/9 = -0.\overline{1}$	-0.1	oil-in-water
Low Ratio	$1.\overline{1}$	$1/10 = 0.1$	$0.\overline{1}$	water-in-oil
High Ratio	1.6	$3/8 = 0.375$	0.6	water-in-pentane

3.2. Droplet Detection Algorithm

The evaluation of the droplet distribution plays a central role in this work. We use a floodfill algorithm to detect the droplets in the VoF field. In the context of this work, we determine the smallest occurring diameter in the statistical distribution of droplets using the criterion suggested by Ling et al. [29], and define $d_{min} = 4L/N$. Droplets with diameters smaller than d_{min} are not resolved well enough by the VoF method [29]. Therefore, they are not included in the statistical distribution.

3.3. Forcing Method and Procedure of the Simulation

To generate a turbulent emulsion in HIT, we use Lundgren linear forcing [19] extended by a PID controller, see Begemann et al. [9]. Figure 1 summarizes the procedure of the simulations. First, we perform a single-phase forcing until a statistically steady state is reached for the carrier phase, as shown in Figure 1a. After inserting the dispersed phase in the form of droplets (see Figure 1b), the emulsion is generated due to the forcing (see Figure 1c). In this process, the TKE k, is kept constant. In the last step, the forcing is turned off, the gravitational acceleration g, is activated, to trigger the segregation process, and slip walls are prescribed in the direction of the gravitational acceleration, as can be seen in Figure 1d,e.

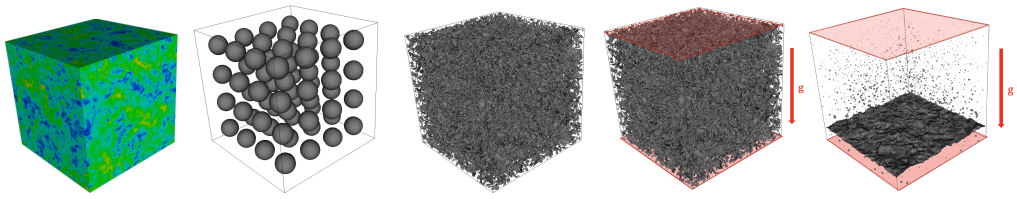

(**a**) (**b**) (**c**) (**d**) (**e**)

Figure 1. Simulation setup: (**a**) single-phase forcing, (**b**) initialization of the droplets of the disperse phase, (**c**) turbulent emulsion in the statistically steady state, (**d**) deactivation of the forcing, switching on of the gravitational acceleration, and prescription of slip walls in the direction of the gravitational acceleration (red walls), (**e**) segregation of the emulsion caused by the gravitational acceleration, g.

4. Effect of Density Ratio on Emulsions

In this section, the influence of the density ratio on the emulsions in the steady state is investigated. To demonstrate the influence of ρ_d/ρ_c, the droplet size distributions and the average interface area are studied and compared.

4.1. Emulsification

First, we study the emulsification under the linear forcing, on the example of the reference case. In Figure 2, the emulsification process of the *Refcase* is visualized. The deformation and subsequent breakup of the initialized droplets can be seen. In the beginning, we observe a significant change in the interface area, while from $t/\tau = 1.0$ onward, only slight changes can be perceived.

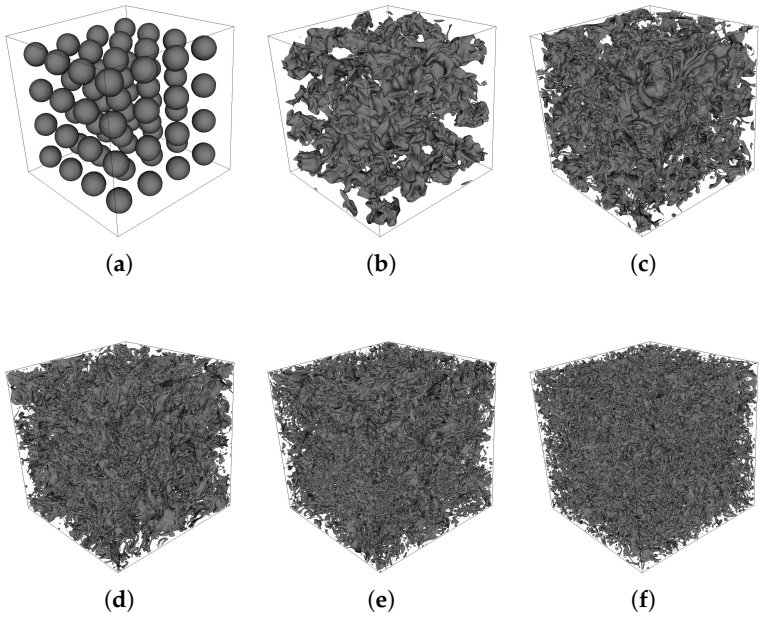

Figure 2. Visualization of the emulsification process of the reference case, from $t/\tau = 0$ to $t/\tau = 2.0$. (**a**) $t/\tau = 0$; (**b**) $t/\tau = 0.25$; (**c**) $t/\tau = 0.5$; (**d**) $t/\tau = 0.75$; (**e**) $t/\tau = 1.0$; (**f**) $t/\tau = 2.0$.

Figure 3 shows the interface area A, normalized by A_∞, of the configuration *Refcase*, over the time, normalized by the eddy turn-over time. Begemann et al. [9] have already demonstrated that, with a Lundgren forcing enhanced by a PID controller, the emulsification process takes about the same time for different configurations and is finished at about $t/\tau \approx 3.0$, as shown for the reference case in Figure 3. Statistical averaging for the subsequent analyses has been performed from $t/\tau = 3.0$ to $t/\tau = 10.0$. In the following, we study the droplet size distribution and the average interface area, to assess the effect of the density difference.

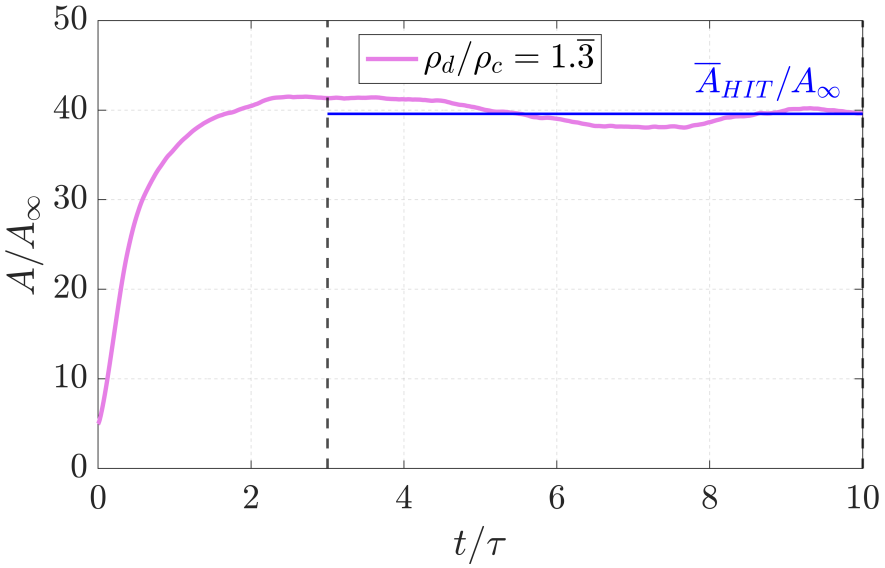

Figure 3. Evolution of the normalized interface area A/A_∞, of the reference case, over the normalized time, t/τ. The first vertical line is the time at which the statistically stationary mixing state is reached. The horizontal line (blue) is the mean value of the normalized interface area $\overline{A}_{HIT}/A_\infty$, between $t/\tau = 3$ and $t/\tau = 10$.

4.2. Droplet Size Distribution

In this section, we discuss the statistical distribution of droplet sizes as a function of the density ratio, and scaling laws are validated. According to Deane and Stokes [7], the distribution of bubbles in breaking waves follows specific laws, the application of which is also discussed for droplets. The Hinze scale represents the most stable maximum droplet diameter. The distribution of bubbles smaller than the Hinze scale is given in the probability density function (PDF) by the power $p_1 \approx -3/2$. Bubbles at the sub-Hinze scale merge with others but rarely fragment because of the larger surface tension forces [7]. This power law was also observed for emulsions in later works [10,17]. Once the bubble size is larger than the Hinze scale, breakup of the individual bubbles becomes more likely. The Weber number thereby increases, and once the critical Weber number, We_{crit}, is exceeded, the breakup processes dominate, because the inertial forces dominate over the surface forces. These bubbles now scale with power $p_2 \approx -10/3$, according to Garret et al. [8], which has also been observed in experiments [41] and numerical studies [10] of emulsions.

Figure 4 shows the droplet size PDFs. Firstly, we observe that, for droplets larger than the Hinze scale, as expected, the breakup of the droplets intensifies and thus the curve becomes steeper. However, a deviation from the scaling law of Garret et al. [8] can be seen in the range $d > d_H$, while in the sub-Hinze range ($d < d_H$), the scaling law of Deane and Stokes [7] remains approximately valid. When analyzing the PDFs with regard to a comparison with the results of Deane and Stokes [7] and Garret et al. [8], it should be noted that the considered configurations exhibit a volume fraction of 12.5%. For volume fractions of dispersion above 10%, a shift of the dominant processes towards coalescence is suspected, as the probability of two droplets merging increases with decreasing distance between the droplets. This effect was mentioned in the numerical works of Crialesi-Esposito et al. [10] and Mukherjee et al. [17].

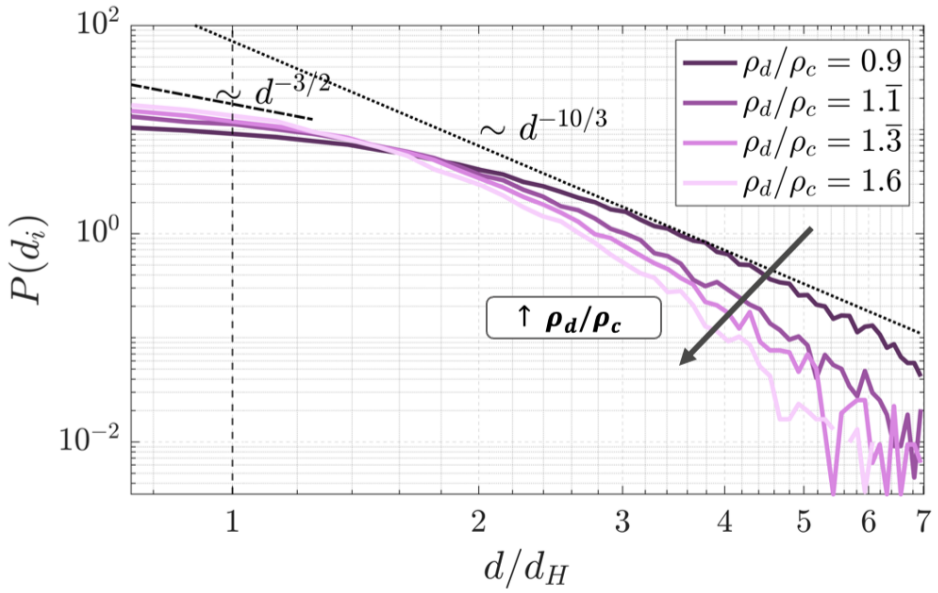

Figure 4. Drop size distribution of the different density ratios together with the scaling laws of Deane and Stokes [7] and Garret et al. [8].

Furthermore, we find that the laws of Deane and Stokes [7] hold better in the sub-Hinze range ($d < d_H$) with increasing density ratio. For droplets larger than the Hinze scale, the distributions are not curved, with a clear asymptotic behavior. The distributions for high density ratios attain a slope of $-10/3$ roughly, at $d/d_h \approx 2$, whereas for smaller density ratios, this slope is reached somewhat later (i.e., $d/d_h \approx 3$). It should be mentioned that these laws were established for small volume fractions of the dispersed phase and a density ratio of 1000, since air bubbles in refracting waves were studied. This fact explains

the convergence of the distribution curves to the scaling law of Deane and Stokes [7] with increasing density ratio.

4.3. Effect on Interface Area and Sauter Mean Diameter

To evaluate the influence of the density ratio on the emulsions, we consider the average interface area A_{HIT}, of the different configurations. Figure 5a compares these values and reveals that the average interface area in the statistically steady state increases with the density ratio. This is in agreement with the PDFs, since we observed that the droplets become smaller with increasing density ratio (see Section 4.2). The interface area also directly affects the SMD

$$d_{32} = \frac{6V_d}{\overline{A}_{HIT}}. \tag{7}$$

The values of the SMDs are shown in Figure 5b.

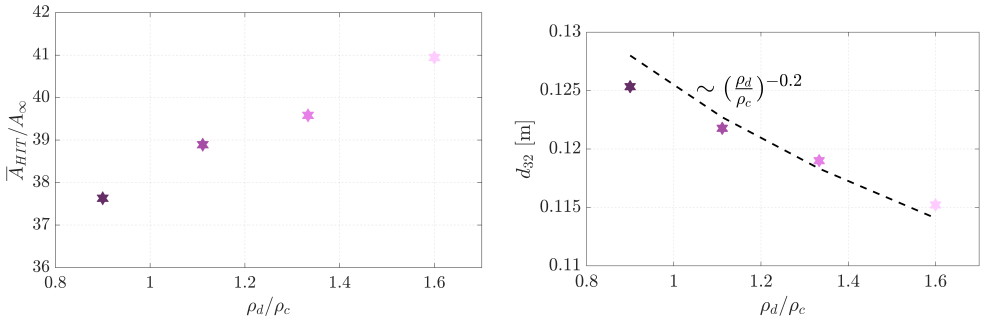

(a) **(b)**

Figure 5. Evolution of (**a**) the normalized interface area $\overline{A}_{HIT}/A_\infty$, of the configurations over ρ_d/ρ_c, and (**b**) the SMD d_{32} over the density ratio ρ_d/ρ_c, together with the scaling law $(\rho_d/\rho_c)^{-0.2}$. The color code corrresponds to Figure 4, i.e., from dark to light color $\rho_d/\rho_c = 0.9, 1.1\bar{1}, 1.3\bar{3}, 1.6$.

It can be concluded that droplets in emulsions with a larger density ratio, break more frequently than those with a smaller density ratio, which implies that the turbulent shear stresses of the turbulence have a stronger effect at larger density ratios. In addition to this, we believe the droplets lose stability at higher density ratios, due to the larger inertial and momentum forces, and break apart earlier. Due to the earlier breakup of the droplets at higher density ratios, the critical Weber number is assumed to be larger at lower density ratios. This observation is in agreement with the concept of the modified critical Weber number, introduced by Levich [42]. Levich [42] and Hesketh et al. [43] derived the following equation for the Hinze scale for liquid–liquid dispersions in horizontal pipelines:

$$d_H^* = \left(\frac{We_{d,crit}}{2}\right)^{3/5}\left(\frac{\rho_c}{\sigma}\right)^{-3/5}\epsilon^{-2/5}\left(\frac{\rho_d}{\rho_c}\right)^{-1/5} = d_H\left(\frac{\rho_d}{\rho_c}\right)^{-1/5}. \tag{8}$$

This equation indicates that, at constant carrier phase density, the Hinze scale is proportional to $(\rho_d/\rho_c)^{-0.2}$. As shown in Figure 5b, the SMDs of the considered cases approximately scale with $(\rho_d/\rho_c)^{-0.2}$, which supports the idea of a density-ratio-dependent critical Weber number.

5. Segregation Process

In order to study the segregation, we switch off the forcing, activate the gravitational acceleration, and prescribe slip walls in the direction of gravitational acceleration. We characterize the segregation process in terms of the height of the center of mass of the disperse phase h_d, its change over time $\dot{h}_d$, and the energy release that drives the segregation process. Further, we apply the segregation time scale proposed by Trummler et al. [15]. We here consider a time t, starting as soon as the forcing is stopped. The gravitational acceleration is chosen to be constant, with $g = 4.59\,\mathrm{m/s^2}$, following [15].

Figure 6 visualizes the segregation process of the considered configurations. By terminating the forcing, the energy supply to the emulsions is withdrawn. The emulsions become unstable and start to segregate. As expected, segregation is promoted for a higher density difference $\Delta\rho$, due to a higher buoyancy force. Especially at $t = 20\,\mathrm{s}$ (see Figure 6a–d(iv)), the influence of $\Delta\rho/\rho_d$ becomes clear. While the configurations *Reverse-Low Ratio* and *Low Ratio* are still in the segregation process, a nearly equilibrium interface is clearly visible at *High Ratio*, and segregation is almost finished. Between *Reverse-Low Ratio* and *Low Ratio*, no significant difference in the temporal course of the segregation process can be noticed.

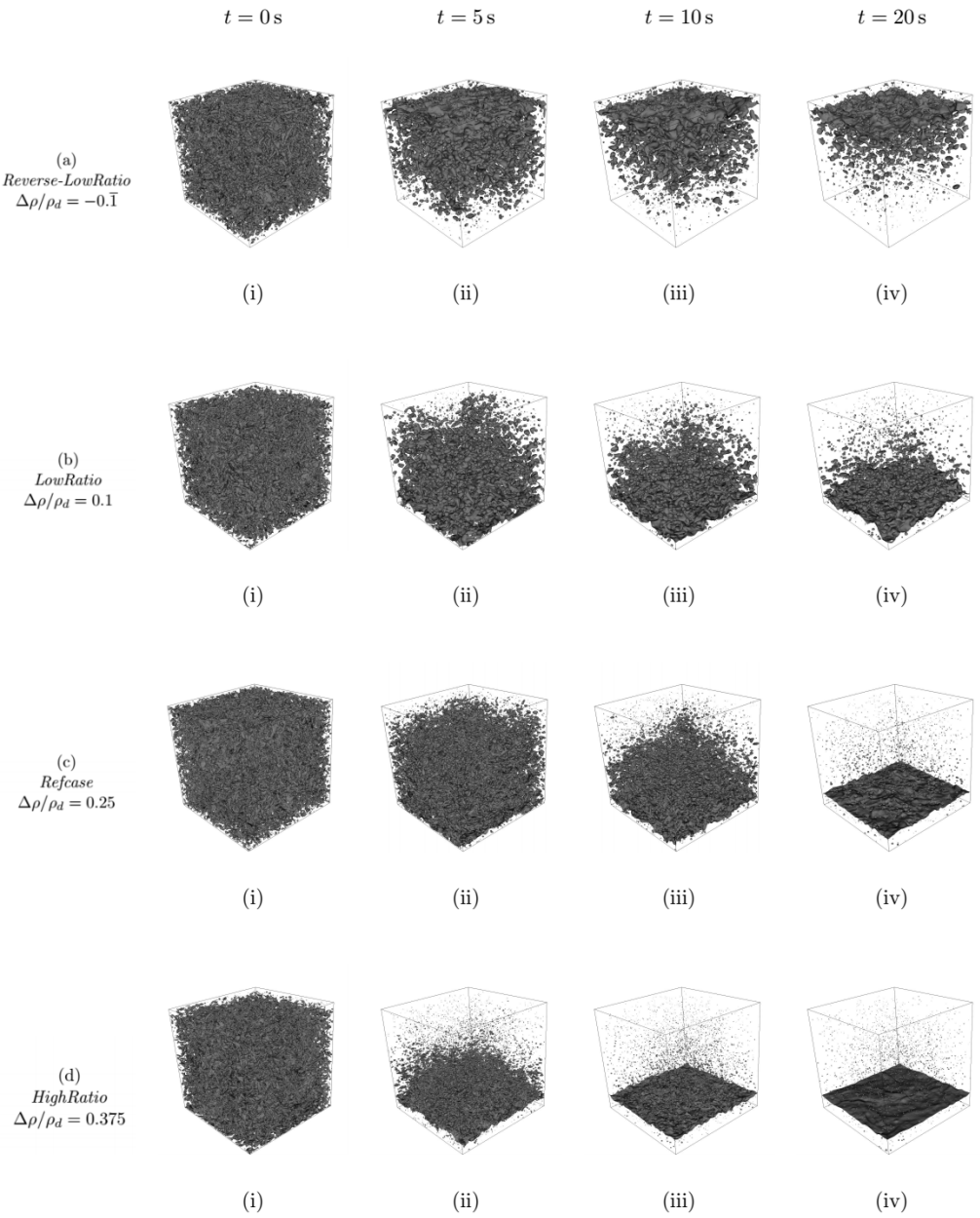

Figure 6. Visualization of the segregation process for varying $\Delta\rho/\rho_d$. The rows correspond to the considered configurations: (**a**) *Reverse-Low Ratio*, (**b**) *Low Ratio*, (**c**) *Refcase*, (**d**) *High Ratio*. The columns correspond to four different time instants subsequent to the start of segregation: (i–iv) corresponds to $t = \{0, 5, 10, 20\}$ s, respectively.

Figure 7 illustrates the height of the center of mass of the dispersed phase as a function of time. Note that the graph of $\Delta\rho/\rho_d = -0.\overline{1}$ is mirrored at $h_d/L = 0.5$, to allow for a

better comparison. In the configurations studied, the segregation progress can be well described by h_d, see [15].

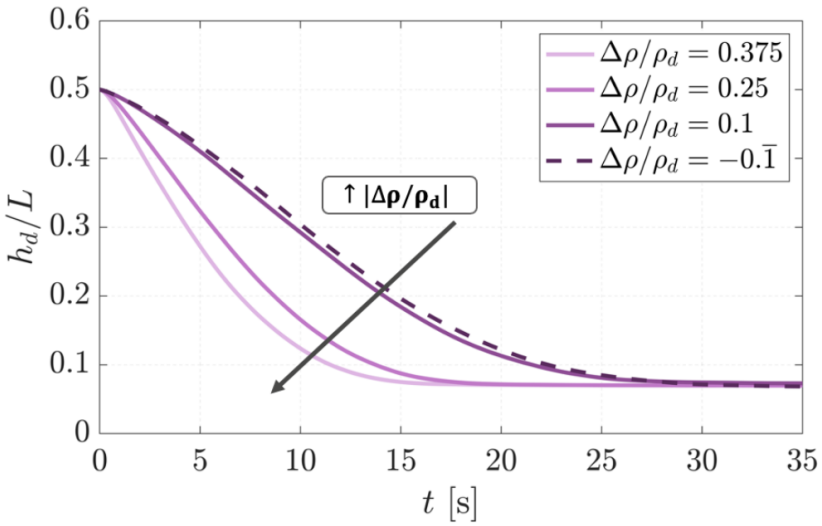

Figure 7. Segregation progress measured by the height of the center of mass of the dispersed phase. Note that the curve of $\Delta\rho/\rho_d = -0.\overline{1}$ is mirrored at $h_d/L = 0.5$, to allow for a better comparison.

In general, the segregation process of non-iso-density emulsions is driven by the minimization of potential energy and surface energy, resulting in the descent of the heavier phase (rising of the lighter phase) and the coalescence of droplets. In the following, we compare the energy release rates of the respective energies, which read

$$\dot{E}_{pot} = \Delta\rho V_d \dot{h}_d g, \quad \dot{E}_\sigma = \sigma \dot{A}. \tag{9}$$

$\dot{h}_d$ is the temporal derivative of the center of mass of the disperse phase. Figure 8 compares the magnitude of the energy release rates for the considered configurations. For all configurations, $\dot{E}_{pot}$ is significantly higher than $\dot{E}_\sigma$, which indicates that the segregation is dominantly driven by gravity and consequently the release of potential energy. $\dot{E}_{pot}$ scales with the density difference $\Delta\rho$ and $\dot{h}_d$, where the latter is also enhanced for a higher $\Delta\rho$. $\dot{E}_\sigma$ is comparable for all configurations, due to the identical surface tension coefficient and a comparable $\dot{A}$.

Finally, we aim to study the time scale of the segregation progress and the effect of the density difference on it. Recently, Trummler et al. [15] proposed a characteristic time scale for gravity-driven segregation processes. They proposed that the average rising/falling of the disperse phase

$$\dot{h}_d^* = c_p U_g \xi(d)\,, \tag{10}$$

scales with the gravity-based velocity

$$U_g = \sqrt{\frac{1}{2}\frac{\Delta\rho}{\rho_d} g H}\,, \tag{11}$$

a proportionality factor c_p and a droplet-size dependent factor $\xi(d)$. Thus, the time scale being inversely proportional to $\dot{h}_d^*$, reads

$$\tau_{seg} = \frac{H}{\dot{h}_d^*} = \frac{1}{c_p}\sqrt{\frac{2(\rho_d/\Delta\rho)H}{g}}\xi(d)^{-1}. \tag{12}$$

H denotes the characteristic change in potential height of the dispersed phase during segregation and is calculated as $H = (1 - 0.5\phi)L - 0.5L = 0.5(1-\phi)L$, which is $H = 7/8\pi$

for the considered setup. The normalization with the proposed time scale resulted in a very good agreement of the temporal evolution of the segregation height for configurations with different gravitational accelerations and surface tension coefficients [15]. For the latter, the factor $\xi(d)$ plays a central role, since the surface tension coefficient alters the droplet size distribution. This term has been approximated with $\xi(d) = (d/d_{ref})^{\gamma}$, where $\gamma = 0.5$ and $d = d_H$.

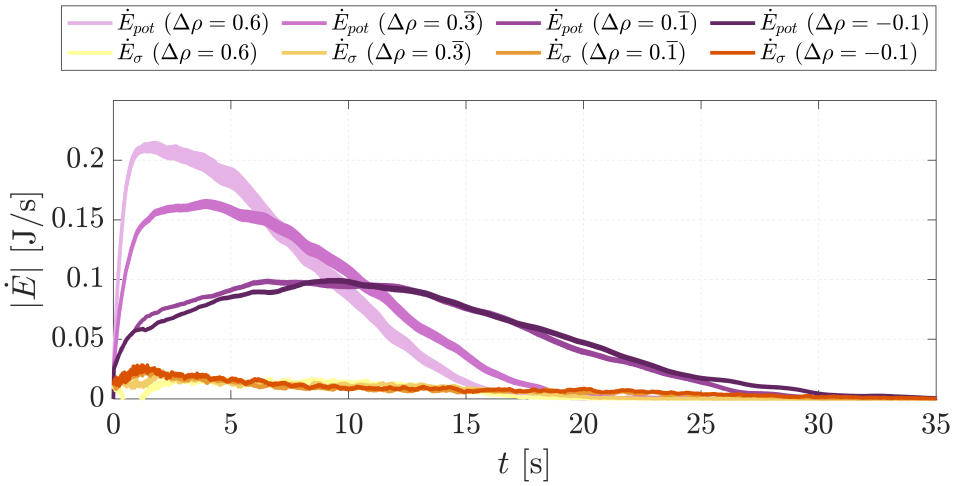

Figure 8. Magnitudes of the energy release rates due to the reduction in the net potential height $\dot{E}_{pot}$, and the reduction in the interface area $\dot{E}_{\sigma}$.

Considering Equation (12), the characteristic time scale for the segregation scales with the square root of the density difference

$$\tau_{seg} \propto \sqrt{\rho_d/\Delta\rho}\,, \tag{13}$$

or respectively

$$\dot{h}_d \propto \sqrt{\Delta\rho/\rho_d}\,. \tag{14}$$

Comparing this expression with Figures 9 and 10a, shows that this approximation yields a good estimate for the effect of the density difference.

In order to directly evaluate the time scale, building on the previous work [15], we use the correlation

$$\dot{h}_d^* = c_p U_g \xi(d), \tag{15}$$

however, we take the SMD as the characteristic diameter, instead of the Hinze scale. We recommend d_{32} at this point, because a dependence of this diameter on the density ratio has been demonstrated in Section 4. In addition, d_{32} is easier to determine in experimental work, whereas the Hinze scale is difficult to estimate, since the dissipation rate and TKE must be known. This gives the equation

$$\dot{h}_d^* = c_p U_g \xi(d) = c_p \sqrt{\frac{1}{2}\frac{\Delta\rho}{\rho_d} g H} \left(\frac{d_{32}}{d_{ref}}\right)^{\gamma}. \tag{16}$$

As the reference diameter d_{ref}, we choose the SMD d_{32}^{REF} of the reference case. c_p and γ have been fitted to the values 0.12 and 0.1. The normalized change in height is plotted in Figure 9.

Consequently, the evaluated time scales are

$$\tau_{seg}^* = \frac{1}{c_p} \sqrt{\frac{2(\rho_d/\Delta\rho)H}{g}} \left(\frac{d_{32}}{d_{ref}}\right)^{-\gamma}. \tag{17}$$

Figure 10 compares the temporal evolution of h_d/L over time, with the one scaled with the derived time scale.

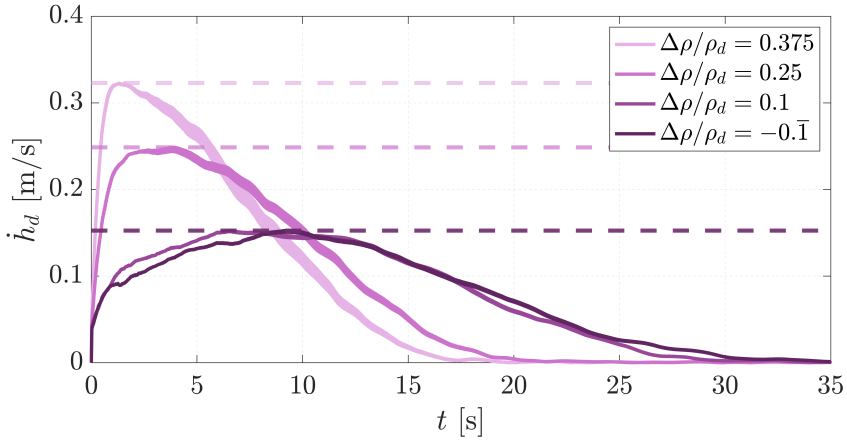

Figure 9. The time derivative of the center of mass of the dispersed phase $\dot{h}_d$. The horizontal lines, with the same color code as the solid lines, correspond to the respective maxima of $\dot{h}_d$.

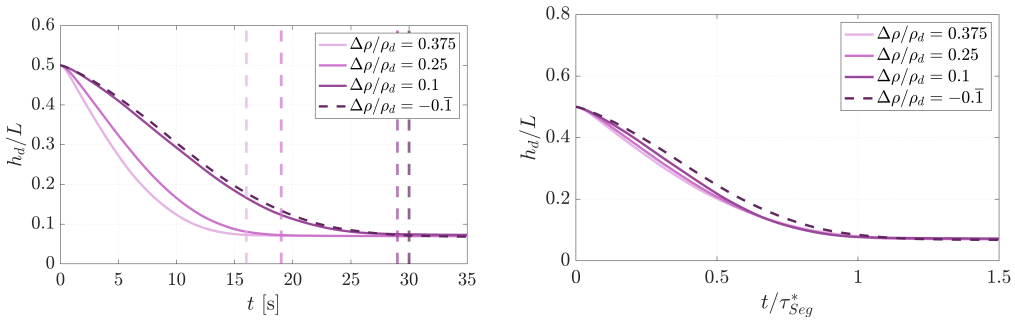

(**a**) (**b**)

Figure 10. Temporal evolution of h_d/L over time in (**a**), and over the normalized time in (**b**). The vertical lines, with the same color code as the solid lines, in (**a**) represent the respective time t_{seg}, at which the segregation is complete.

We recognize that the scaling with τ^*_{seg} is very accurate. For all cases considered, $t_{seg}/\tau^*_{seg} \approx 1$ is valid and the lines are also close to each other.

6. Conclusions

In this work we analyzed turbulent emulsions using DNS, in a statistically steady state, and evaluated their segregation. In order to achieve this, homogeneous isotropic turbulence was generated using an extended linear forcing method, that accounted for the additional surface tension contribution in the turbulent kinetic energy balance equation. When the steady state was reached, the forcing was stopped, and gravitational acceleration was activated. The proposed computational setup represents a well-controlled configuration to study emulsification and segregation.

The density ratio has a significant influence on the formation of emulsions. Using the interface area and the SMD, we have confirmed that an increasing density ratio in emulsions, at statistically stationary state, leads to larger droplets. Moreover, we observed that the SMD approximately scales with $(\rho_d/\rho_c)^{-0.2}$, which supports the suggestions of Levich [42] and Hesketh et al. [43]. The power laws of Deane and Stokes [7] and Garret et al. [8], are in limited agreement with our results and require further discussion for higher volume fractions and different density ratios. Due to the lower stability of the droplets at higher density ratios, and the dependence of the SMD on the density ratio, a

dependence of the critical Weber number and the Hinze scale on the density ratio are also suspected, a theory already put forward by Levich [42].

For segregation, an increasing $\Delta\rho/\rho_d$ leads to a faster segregation. The change in potential energy also becomes stronger, while the change in surface energy remains almost the same. However, the smaller droplets present for increasing density ratios hinder these processes, so that the segregation does not scale ideally with $\Delta\rho/\rho_d$. Smaller droplets also reduce the influence of the potential energy change relative to the change in surface energy, driving the segregation process. As a result, a moderate difference can be observed, depending on whether the disperse phase is lighter or heavier than the carrier phase. Furthermore, the time scale for segregation introduced by Trummler [15] was reviewed and modified. In this work, we recommend an estimation with the SMD instead of the Hinze scale, and derive a new time scale τ^*_{seg}, which proved to be very accurate and accurately collapses the height of the center of mass for different density ratios. The segregation time must also be investigated experimentally, to validate the proposed time scale. The coalescence processes of droplets during the segregation should also be studied further, to improve the understanding of segregation and enable its mathematical modeling.

Author Contributions: Conceptualization, O.K. and T.T.; methodology, O.K., E.T., T.T. and M.K.; software, O.K., E.T. and T.T.; formal analysis, O.K.; investigation, O.K., T.T. and M.K.; resources, M.K.; writing—original draft preparation, O.K.; writing—review and editing, O.K., E.T., T.T. and M.K.; visualization, O.K.; supervision, T.T. and M.K.; project administration, T.T. and M.K.; funding acquisition, M.K. All authors have read and agreed to the published version of the manuscript.

Funding: This project received funding from *dtec.bw*—Digitalization and Technology Research Center of the Bundeswehr—under the project *MORE*, which is gratefully acknowledged. *dtec.bw* is funded by the European Union—NextGenerationEU.

Data Availability Statement: The data that support the findings of this study are available from the corresponding author upon reasonable request

Acknowledgments: The authors thank the Gauss Centre for Supercomputing e.V. (www.gauss-centre.eu) for providing computing time on the GCS Supercomputer SuperMUC-NG, at the Leibniz Supercomputing Centre (www.lrz.de). We acknowledge financial support by Universität der Bundeswehr München.

Conflicts of Interest: The authors declare that they have no known competing financial interest or personal relationship that could have appeared to influence the work reported in this paper.

Abbreviations

The following abbreviations are used in this manuscript:

CSF	Continuous surface force
CFD	Computational fluid dynamics
DNS	Direct numerical simulation
GWDI	Gasoline-water direct injection
HIT	Homogeneous isotropic turbulence
PARIS	Parallel, robust, interface simulator
PDF	Probability density function
PID	Proportional–integral–derivative (controller)
QUICK	Quadratic upstream interpolation for convective kinematics
SMD	Sauter mean diameter
SOR	Successive over-relaxation
TKE	Turbulent kinetic energy
VoF	Volume of fluid method

References

1. Spernath, A.; Aserin, A. Microemulsions as carriers for drugs and nutraceuticals. *Adv. Colloid Interface Sci.* **2006**, *128*, 47–64. [CrossRef] [PubMed]

2. Guzey, D.; McClements, D.J. Formation, stability and properties of multilayer emulsions for application in the food industry. *Adv. Colloid Interface Sci.* **2006**, *128*, 227–248. [CrossRef] [PubMed]
3. Angardi, V.; Ettehadi, A.; Yücel, Ö. Critical Review of Emulsion Stability and Characterization Techniques in Oil Processing. *J. Energy Resour. Technol.* **2022**, *144*, 040801. [CrossRef]
4. Wang, Z.; Bai, Y.; Zhang, H.; Liu, Y. Investigation on gelation nucleation kinetics of waxy crude oil emulsions by their thermal behavior. *J. Pet. Sci. Eng.* **2019**, *181*, 106230. [CrossRef]
5. Wang, Z.; Xu, Y.; Khan, N.; Zhu, C.; Gao, Y. Effects of the surfactant, polymer, and crude oil properties on the formation and stabilization of oil-based foam liquid films: Insights from the microscale. *J. Mol. Liq.* **2023**, *373*, 121194. [CrossRef]
6. Heinrich, C.; Dörksen, H.; Esch, A.; Krämer, K. Gasoline water direct injection (GWDI) as a key feature for future gasoline engines. In Proceedings of the International Conference on Knocking in Gasoline Engines, Berlin, Germany, 12–13 December 2017; pp. 322–337.
7. Deane, G.B.; Stokes, M.D. Scale dependence of bubble creation mechanisms in breaking waves. *Nature* **2002**, *418*, 839–844. [CrossRef]
8. Garrett, C.; Li, M.; Farmer, D. The connection between bubble size spectra and energy dissipation rates in the upper ocean. *J. Phys. Oceanogr.* **2000**, *30*, 2163–2171. [CrossRef]
9. Begemann, A.; Trummler, T.; Trautner, E.; Hasslberger, J.; Klein, M. Effect of turbulence intensity and surface tension on the emulsification process and its stationary state—A numerical study. *Can. J. Chem. Eng.* **2022**, *100*, 3548–3561. [CrossRef]
10. Crialesi-Esposito, M.; Rosti, M.E.; Chibbaro, S.; Brandt, L. Modulation of homogeneous and isotropic turbulence in emulsions. *J. Fluid Mech.* **2022**, *940*, A19. [CrossRef]
11. Pacek, A.; Man, C.; Nienow, A. On the Sauter mean diameter and size distributions in turbulent liquid/liquid dispersions in a stirred vessel. *Chem. Eng. Sci.* **1998**, *53*, 2005–2011. [CrossRef]
12. Kraume, M.; Gäbler, A.; Schulze, K. Influence of physical properties on drop size distribution of stirred liquid-liquid dispersions. *CHemical Eng. Technol.: Ind. Chem.-Plant Equip.-Process Eng.-Biotechnol.* **2004**, *27*, 330–334. [CrossRef]
13. Koegl, M.; Mull, C.; Mishra, Y.N.; Will, S.; Zigan, L. Characterization of fuel/water mixtures and emulsions with ethanol using laser-induced fluorescence. *Appl. Opt.* **2020**, *59*, 1136–1144. [CrossRef] [PubMed]
14. Frising, T.; Noïk, C.; Dalmazzone, C. The liquid/liquid sedimentation process: From droplet coalescence to technologically enhanced water/oil emulsion gravity separators: A review. *J. Dispers. Sci. Technol.* **2006**, *27*, 1035–1057. [CrossRef]
15. Trummler, T.; Begemann, A.; Trautner, E.; Klein, M. Numerical investigation of the segregation of turbulent emulsions. *Phys. Fluids* **2022**, *34*, 113324. [CrossRef]
16. Perlekar, P.; Biferale, L.; Sbragaglia, M.; Srivastava, S.; Toschi, F. Droplet size distribution in homogeneous isotropic turbulence. *Phys. Fluids* **2012**, *24*, 065101. [CrossRef]
17. Mukherjee, S.; Safdari, A.; Shardt, O.; Kenjereš, S.; Van den Akker, H.E. Droplet–turbulence interactions and quasi-equilibrium dynamics in turbulent emulsions. *J. Fluid Mech.* **2019**, *878*, 221–276. [CrossRef]
18. Dodd, M.S.; Ferrante, A. On the interaction of Taylor length scale size droplets and isotropic turbulence. *J. Fluid Mech.* **2016**, *806*, 356–412. [CrossRef]
19. Lundgren, T. *Linearly Forced Isotropic Turbulence, Annual Research Briefs*; Technical report 461; Center for Turbulence Research: Stanford, CA, USA, 2003.
20. Carroll, P.L.; Blanquart, G. A proposed modification to Lundgren's physical space velocity forcing method for isotropic turbulence. *Phys. Fluids* **2013**, *25*, 105114. [CrossRef]
21. Shao, C.; Luo, K.; Yang, Y.; Fan, J. Direct numerical simulation of droplet breakup in homogeneous isotropic turbulence: The effect of the Weber number. *Int. J. Multiph. Flow* **2018**, *107*, 263–274. [CrossRef]
22. Skartlien, R.; Sollum, E.; Schumann, H. Droplet size distributions in turbulent emulsions: Breakup criteria and surfactant effects from direct numerical simulations. *J. Chem. Phys.* **2013**, *139*, 174901. [CrossRef]
23. Aniszewski, W.; Arrufat, T.; Crialesi-Esposito, M.; Dabiri, S.; Fuster, D.; Ling, Y.; Lu, J.; Malan, L.; Pal, S.; Scardovelli, R.; et al. Parallel, robust, interface simulator (PARIS). *Comput. Phys. Commun.* **2021**, *263*, 107849. [CrossRef]
24. Prosperetti, A.; Tryggvason, G. *Computational Methods for Multiphase Flow*; Cambridge University Press: Cambridge, UK, 2009.
25. Hirt, C.W.; Nichols, B.D. Volume of fluid (VOF) method for the dynamics of free boundaries. *J. Comput. Phys.* **1981**, *39*, 201–225. [CrossRef]
26. Brackbill, J.U.; Kothe, D.B.; Zemach, C. A continuum method for modeling surface tension. *J. Comput. Phys.* **1992**, *100*, 335–354. [CrossRef]
27. Popinet, S. An accurate adaptive solver for surface-tension-driven interfacial flows. *J. Comput. Phys.* **2009**, *228*, 5838–5866. [CrossRef]
28. Leonard, B.P. A stable and accurate convective modelling procedure based on quadratic upstream interpolation. *Comput. Methods Appl. Mech. Eng.* **1979**, *19*, 59–98. [CrossRef]
29. Ling, Y.; Zaleski, S.; Scardovelli, R. Multiscale simulation of atomization with small droplets represented by a Lagrangian point-particle model. *Int. J. Multiph. Flow* **2015**, *76*, 122–143. [CrossRef]
30. Ling, Y.; Fuster, D.; Zaleski, S.; Tryggvason, G. Spray formation in a quasiplanar gas-liquid mixing layer at moderate density ratios: A numerical closeup. *Phys. Rev. Fluids* **2017**, *2*, 014005. [CrossRef]

31. Ketterl, S.; Klein, M. A Band-Width Filtered Forcing Based Generation of Turbulent Inflow Data for Direct Numerical or Large Eddy Simulations and its Application to Primary Breakup of Liquid Jets. *Flow Turbul. Combust.* **2018**, *101*, 413–432. [CrossRef]
32. Hasslberger, J.; Ketterl, S.; Klein, M.; Chakraborty, N. Flow topologies in primary atomization of liquid jets: A direct numerical simulation analysis. *J. Fluid Mech.* **2019**, *859*, 819–838. [CrossRef]
33. Ling, Y.; Fuster, D.; Tryggvason, G.; Zaleski, S. A two-phase mixing layer between parallel gas and liquid streams: Multiphase turbulence statistics and influence of interfacial instability. *J. Fluid Mech.* **2019**, *859*, 268–307. [CrossRef]
34. Crialesi-Esposito, M.; Gonzalez-Montero, L.; Salvador, F. Effects of isotropic and anisotropic turbulent structures over spray atomization in the near field. *Int. J. Multiph. Flow* **2022**, *150*, 103891. [CrossRef]
35. Trautner, E.; Hasslberger, J.; Ketterl, S.; Klein, M. Primary atomization of liquid jets: Identification and investigation of droplets at the instant of their formation using direct numerical simulation. *Int. J. Multiph. Flow* **2023**, *160*, 104360. [CrossRef]
36. Hinze, J.O. Fundamentals of the hydrodynamic mechanism of splitting in dispersion processes. *AIChE J.* **1955**, *1*, 289–295. [CrossRef]
37. Yi, L.; Toschi, F.; Sun, C. Global and local statistics in turbulent emulsions. *J. Fluid Mech.* **2021**, *912*, A13. [CrossRef]
38. Rosales, C.; Meneveau, C. Linear forcing in numerical simulations of isotropic turbulence: Physical space implementations and convergence properties. *Phys. Fluids* **2005**, *17*, 095106. [CrossRef]
39. Pope, S.B. Book review: Turbulent flows. *Meas. Sci. Technol.* **2001**, *12*, 2020–2021. [CrossRef]
40. Wagner, T.; Rottengruber, H.; Beyrau, F.; Dragomirov, P.; Schaub, M. Measurement of a Direct Water-Gasoline-Emulsion-Injection. In Proceedings of the Ilass Europe 28th European Conference on Liquid Atomization and Spray Systems, València, Spain, 6–8 September 2017; pp. 330–338.
41. Qi, Y.; Masuk, A.U.M.; Ni, R. Towards a model of bubble breakup in turbulence through experimental constraints. *Int. J. Multiph. Flow* **2020**, *132*, 103397. [CrossRef]
42. Levich, V.G. *Physicochemical Hydrodynamics*, 1st ed.; Prentice-Hall: Englewood Cliffs, NJ, USA, 1962.
43. Hesketh, R.; Etchells, A.; Russell, T.F. Bubble size in horizontal pipelines. *AIChE J.* **1987**, *33*, 663. [CrossRef]